

# The dynamic response of seabed anchored floating tunnels under seismic excitation

P. Fogazzi and F. Perotti<sup>\*,†</sup>

*Dipartimento di Ingegneria Strutturale, Politecnico di Milano, Piazza Leonardo da Vinci 32, Milan 20133, Italy*

## SUMMARY

In this paper a procedure for analysing the seismic response of seabed anchored floating tunnels is presented. The first step of the research was the development of an 'ad hoc' finite element for modelling the behaviour of anchor elements, with particular reference to the problem of transverse oscillations under time varying axial loads. The element was subsequently inserted in a step-by-step procedure for the numerical analysis of non-linear response to multiple-support seismic input; the procedure encompasses simplified modelling of fluid–structure and soil–structure interaction effects. An example of an application is given concerning two 4680 m long floating tunnels with different seabed profiles. Copyright © 2000 John Wiley & Sons, Ltd.

KEY WORDS: submerged structures; non-linear structural dynamics; multiple-support seismic excitation

## 1. INTRODUCTION

Seabed anchored floating tunnels seem to be a promising alternative to long-span bridges and underground tunnels for fjord, lake and sea-strait crossing. The behaviour of such structures when subjected to extreme loading conditions, however, involves delicate design and computational questions (see Brancaloni *et al.* [1] for a review of the topic); one of these is represented by the structural response to ultimate seismic actions [2, 3]. The seismic issue, in turn, shows different facets which we will try to summarize, with the help of Figures 1 and 2, as follows.

- (a) The transverse and vertical components of ground motions are mainly resisted by the inclined anchor elements, which usually lie in planes normal to the tunnel axis (Figure 2); depending on the seabed profile (Figure 1) and on other design considerations, these elements can be characterized by slenderness values differing almost by an order of magnitude, thus showing very different behaviours. It must be noted, in this respect, that recent approaches to the tunnel structural design allow for the occurrence of compressive

---

\* Correspondence to: F. Perotti, Dipartimento di Ingegneria Strutturale, Politecnico di Milano, Piazza Leonardo da Vinci 32, Milan 20133, Italy.

† E-mail: perotti@stru.polimi.it

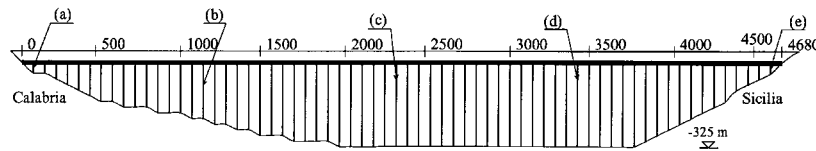


Figure 1. Side view of floating tunnel (Example A).

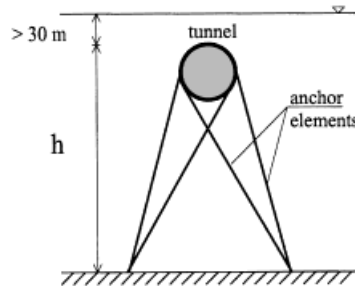


Figure 2. Example of floating tunnel: section at anchor system location.

loads acting upon anchor elements in ultimate conditions; considering that in the example here studied, the largest part of these elements has slenderness values ranging from 300 to 637, it can be easily understood why dynamic stability of the anchor bars has been regarded as a key issue of the seismic behaviour.

- (b) The tunnel response to longitudinal seismic actions is likely to be mainly governed by the behaviour of end restraining systems, unless the geometry of the anchor elements is modified.
- (c) For all excitation components the spatial variation of ground motion appears to be of importance, since the tunnel acts as a continuous beam on deformable supports, this structural configuration being prone to multiple-support excitation effects.
- (d) Floating tunnels are usually designed to be placed at a convenient depth, to minimize the effect of surface sea waves; in seismic conditions, however, vertical waves arising by the motion of the seabed can be of importance for the resistance of the anchoring system

In the research work here presented points (a) and (c) are addressed; the transverse and vertical response of two 'prototype' floating tunnels under multiple-support seismic excitation are studied. To this end a finite element was developed for modelling the dynamic behaviour of the anchor elements; a description of the element properties is given in Section 2. In Section 3 overall strategies for seismic response computation are discussed. In Section 4 the examples of application are given and the obtained results are discussed.

## 2. THE ANCHOR ELEMENT MODEL

The development of an 'ad hoc' finite element to simulate the anchor element behaviour was deemed to be necessary; in fact adoption of existing 'general purpose' procedures leads, for the

problem at study, to the use of beam elements allowing for large displacements and deformations. Moreover, a significant number of elements must be introduced for each anchor rod; when the performance of a number of analyses during the design phase is considered and the possible extension of the study to complete 3-D excitation and to non-linear material behaviour is anticipated, it is clear that the computational cost and time can easily become prohibitive, unless simplifying assumptions are made.

In view of this a new finite element was studied according to the following criteria: (a) capability of modelling the entire structural element; (b) computational efficiency; (c) capability of representing the interaction between time varying axial forces and transverse oscillations; (d) possibility of efficient extension of the model to 3D oscillations and elastic-plastic behaviour.

Note that points (a) and (b) stem from the necessity to model the entire tunnel, which easily encompasses hundreds of anchor elements; as to point (c) this is here of particular significance due to hydrodynamic interaction effects, i.e. inertia forces due to added mass and hydrodynamic damping forces, whose transverse components may significantly affect, in the dynamic non-linear range, the axial loading capacity of the anchor bar.

To meet the above requirements a reasonable compromise between computational efficiency and modelling refinement was sought. As a result a five-degree-of freedom hinged bar plane element was developed; the main features of the element will be discussed in the next sections.

### 2.1. Computation of the stiffness matrix

The element stiffness matrix was computed on the basis of the following assumptions:

- (1) transverse displacements and rotations relative to the bar chord are small;
- (2) axial deformation, which is assumed to be small and constant along the bar, is expressed as a quadratic function of nodal displacements, including the effect of transverse motion;
- (3) elastic material behaviour is assumed.

**2.1.1. Definition of local stiffness.** With reference to the statically determined element shown in Figure 3 the following 'intrinsic' local co-ordinates are introduced:

- (1)  $v_1$  is the axial relative end displacement due to elastic effects, i.e.  $\varepsilon_N = v'_x = v_1/L$  is the constant axial deformation,
- (2)  $v_2$  is the midspan transverse displacement with respect to the element chord, i.e.  $v_2 = v_y(L/2)$ .

Both displacements are assumed to be small;  $v_1$  leads to a small axial strain and  $v_2$  leads to a curvature distribution which can be approximated by the second derivative  $v''_y$ . By introducing a sinusoidal shape function the transverse displacement and the curvature can be expressed as

$$v_y(x) = v_2 \sin\left(\frac{\pi x}{L}\right), \quad \chi(x) = v''_y(x) = -v_2 \left(\frac{\pi}{L}\right)^2 \sin\left(\frac{\pi x}{L}\right) \quad (1)$$

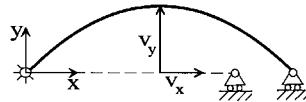


Figure 3. Local 'intrinsic' co-ordinate system for anchor element.

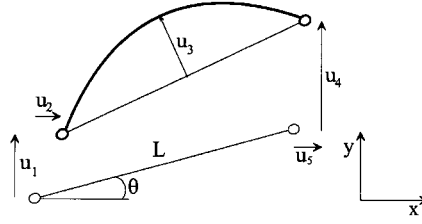


Figure 4. Global co-ordinate system for anchor element.

By introducing the local co-ordinate vector  $\mathbf{v} = \{v_1, v_2\}^T$  and neglecting shear deformations the total strain energy can be expressed in the usual form:

$$\Pi = \frac{1}{2} \int_0^L EA \varepsilon_N^2 dx + \frac{1}{2} \int_0^L EJ \chi^2 dx = \frac{1}{2} \mathbf{v}^T \mathbf{k} \mathbf{v} \quad (2)$$

From Equation (2) and the above statements the local elastic stiffness matrix  $\mathbf{k}$  can be easily defined in the following way:

$$\mathbf{k} = \frac{EJ}{L^3} \begin{bmatrix} \lambda^2 & 0 \\ 0 & \pi^4/2 \end{bmatrix} \quad (3)$$

where  $A$  and  $J$  are the element cross-section area and moment of inertia,  $\lambda$  is the bar slenderness and  $E$  is the material Young modulus.

Multiplication of the local stiffness  $\mathbf{k}$  times the local co-ordinate vector  $\mathbf{v}$  gives the local forces  $N$  (axial force) and  $V$  (generalized force associated to the midspan deflection), i.e.

$$\mathbf{P} = \{N, V\}^T = \mathbf{k} \mathbf{v} \quad (4)$$

It can be noted that the introduction of non-linear material behaviour, presently under development, can be performed at this stage of the formulation, thus leading to the evaluation of a suitable tangent local stiffness.

The element formulation can be also improved, in terms of transverse behaviour, by adding other deformation modes and, accordingly, local co-ordinates.

**2.1.2. Generalized strain-displacement relation.** The  $v_1$  and  $v_2$  local co-ordinates can be regarded as generalized strain components describing, under the above hypotheses, axial and flexural deformations throughout the bar. With reference to Figure 4 local co-ordinates can be related to global (element) ones  $\mathbf{u}$ ;  $u_1, u_2, u_3, u_4, u_5$  are the components of total end displacements in the global reference system, while  $u_3$  is again the midspan transverse displacement relative to the bar chord, which means that the equality  $u_3 = v_2$  holds.

To relate the local co-ordinate  $v_1$  to the  $\mathbf{u}$  displacements, the contributions due to ends displacement and to the effect ('bowing effect') of the transverse motion are treated separately and then superimposed for computing the average axial strain  $v_1/L$ . In this light the first contribution can be expressed, retaining terms up to the 2nd power, as

$$v_1^{(e)} = (u_4 - u_1)s + (u_5 - u_2)c + \frac{1}{2L} [(u_4 - u_1)^2 + (u_5 - u_2)^2] \quad (5)$$

where  $c = \cos \theta$  and  $s = \sin \theta$ ,  $\theta$  being the bar inclination in the undeformed configuration. The effect of the (small) transverse displacement, relative to the chord, can be computed, up to second order and by use of (1), as

$$v_1^{(b)} = \frac{1}{2} \int_0^L v_y'^2 dx = \frac{\pi^2}{4L} u_3^2 \quad (6)$$

By adding the two contributions the total elongation can be obtained as  $v_1 = v_1^{(e)} + v_1^{(b)}$ ; in incremental form the same quantity can be written as

$$\begin{aligned} \Delta v_1 &= v_1(\mathbf{u} + \Delta \mathbf{u}) - v_1(\mathbf{u}) = \left[ \frac{1}{L} (u_1 - u_4) - s \right] \Delta u_1 + \left[ \frac{1}{L} (u_2 - u_5) - c \right] \Delta u_2 \\ &\quad - \left[ \frac{1}{L} (u_1 - u_4) - s \right] \Delta u_4 - \left[ \frac{1}{L} (u_2 - u_5) - c \right] \Delta u_5 + \frac{\pi^2}{2L} u_3 \Delta u_3 \\ &\quad + \frac{1}{2L} \left( \Delta u_1^2 + \Delta u_2^2 + \frac{\pi^2}{2} \Delta u_3^2 + \Delta u_4^2 + \Delta u_5^2 - 2\Delta u_1 \Delta u_4 - 2\Delta u_2 \Delta u_5 \right) \\ &= \Delta \mathbf{u}^T \mathbf{B}_L + \frac{1}{2} \Delta \mathbf{u}^T \mathbf{B}_{NL} \Delta \mathbf{u} \end{aligned} \quad (7)$$

where the linear and non-linear generalized strain-displacement matrices are defined as follows:

$$\mathbf{B}_L^T = \left[ \frac{u_1 - u_4}{L} - s, \quad \frac{u_2 - u_5}{L} - c, \quad \frac{\pi^2}{2L} u_3, \quad -\left( \frac{u_1 - u_4}{L} - s \right), \quad -\left( \frac{u_2 - u_5}{L} - c \right) \right] \quad (8)$$

$$\mathbf{B}_{NL} = \begin{bmatrix} 1 & 0 & 0 & -1 & 0 \\ 0 & 1 & 0 & 0 & -1 \\ 0 & 0 & \frac{\pi^2}{2} & 0 & 0 \\ -1 & 0 & 0 & 1 & 0 \\ 0 & -1 & 0 & 0 & 1 \end{bmatrix} \quad (9)$$

**2.1.3. Computation of element stiffness matrix in the global reference system.** The element was developed to be used within a Lagrangian incremental analysis, in which [4] equilibrium must be imposed at time  $t + \Delta t$  (response at time  $t$  is assumed to be known). To this aim the principle of virtual displacements can be invoked by adopting displacement increments  $\Delta \mathbf{u}$  and strain increments ( $\Delta \varepsilon_N$  and  $\Delta \chi$ ) as kinematic quantities; by equating the internal work to the work done by generalized elastic forces  ${}^{t+\Delta t} \mathbf{F}$  one can write, in the small deformation hypothesis,

$$\delta(\Delta \mathbf{u}^T) {}^{t+\Delta t} \mathbf{F} = \int_0^L \delta(\Delta \varepsilon_N) {}^{t+\Delta t} N dx + \int_0^L \delta(\Delta \chi) {}^{t+\Delta t} M dx \quad (10)$$

Deformation increments can be written, at this point (see Equations (1) and (7)), as

$$\Delta \varepsilon_N = \frac{\Delta v_1}{L} = \frac{1}{L} \left( \Delta \mathbf{u}^T \mathbf{B}_L + \frac{1}{2} \Delta \mathbf{u}^T \mathbf{B}_{NL} \Delta \mathbf{u} \right) \quad (11)$$

$$\Delta \chi = -\Delta v_2 \left( \frac{\pi}{L} \right)^2 \sin \left( \frac{\pi x}{L} \right) = -\Delta u_3 \left( \frac{\pi}{L} \right)^2 \sin \left( \frac{\pi x}{L} \right) \quad (12)$$

where the  $u_j$  co-ordinates appearing in the  $\mathbf{B}_L$  matrix (8) are the values at time  $t$ .

The extension contribution  $W_{i,a}$  to the internal virtual work can be re-written, by incremental decomposition of the axial force, in the following form:

$$W_{i,a} = \int_0^L \delta(\Delta \varepsilon_N) ({}^t N + \Delta N) dx = \frac{1}{L} \int_0^L \delta(\Delta v_1) \Delta N dx + \frac{1}{L} \int_0^L \delta(\Delta v_1) {}^t N dx \quad (13)$$

The first term appearing at the r.h.s. of Equation (13) can be estimated by adopting the usual approximations

$$\delta(\Delta v_1) \cong \delta(\Delta \mathbf{u}^T) \mathbf{B}_L, \quad \Delta N = k_{11} \Delta v_1 \cong k_{11} \mathbf{B}_L^T \Delta \mathbf{u} \quad (14)$$

which lead to the linearized form

$$\frac{1}{L} \int_0^L \delta(\Delta v_1) \Delta N dx \cong \frac{1}{L} \delta(\Delta \mathbf{u}^T) k_{11} \int_0^L \mathbf{B}_L \mathbf{B}_L^T dx \Delta \mathbf{u} \quad (15)$$

As to the second term at the r.h.s. of (13), upon substitution of Equation (11) we write the following:

$$\frac{1}{L} \int_0^L \delta(\Delta v_1) {}^t N dx = \frac{1}{L} \left( \delta(\Delta \mathbf{u}^T) {}^t N \int_0^L \mathbf{B}_L dx + \delta(\Delta \mathbf{u}^T) {}^t N \int_0^L \mathbf{B}_{NL} dx \Delta \mathbf{u} \right) \quad (16)$$

Finally, the flexural contribution  $W_{i,f}$  can be written, by use of Equations (1) and (12) and by incremental decomposition of the bending moment, as

$$W_{i,f} = \int_0^L \delta(\Delta \chi) ({}^t M + \Delta M) dx = (k_{22} \Delta u_3 + {}^t V) \delta(\Delta u_3) \quad (17)$$

where  ${}^t V$  is the generalized component of the elastic force related to co-ordinate  $u_3$  (or  $v_2$ ), evaluated at time  $t$ .

Upon substitution in (10) of Equations (15)–(17) the generalized elastic force at time  $t + \Delta t$  can be estimated through the equation:

$${}^{t+\Delta t} \mathbf{F} = \mathbf{K}_L \Delta \mathbf{u} + \mathbf{K}_{NL} \Delta \mathbf{u} + {}^t \mathbf{F} \quad (18)$$

where the following matrices appear:

$$\mathbf{K}_L = \frac{k_{11}}{L} \int_0^L \mathbf{B}_L \mathbf{B}_L^T dx + \mathbf{K}_{L,f} \quad (19)$$

$$\mathbf{K}_{NL} = \frac{{}^t N}{L} \int_0^L \mathbf{B}_{NL} dx = {}^t N \mathbf{B}_{NL} \quad (20)$$

$${}^t\mathbf{F} = \frac{{}^tN}{L} \int_0^L \mathbf{B}_L dx + \{0, 0, {}^tV, 0, 0\}^T \quad (21)$$

The total element stiffness is thus defined as the sum of the elastic (linearized) stiffness matrix  $\mathbf{K}_L$  and of the geometric stiffness matrix  $\mathbf{K}_{NL}$ , i.e.

$$\mathbf{K} = \mathbf{K}_L + \mathbf{K}_{NL} \quad (22)$$

while  ${}^t\mathbf{F}$  lists generalized elastic forces at time  $t$ . Closed-form expression of  $\mathbf{K}_L$  is given in the Appendix.

Note that, owing to the form of matrix  $\mathbf{B}_L$  (Equation (8)) the elastic matrix depends on the configuration at time  $t$ , while the geometric stiffness is constant (see  $\mathbf{B}_{NL}$ , Equation (9)).

It is also worth noting that, when the local co-ordinate  $u_3$  is restrained, the element reduces to an usual two-node truss element [4] formulated according to the small strain-large rotation conditions.

## 2.2. Computation of generalized elastic forces

Owing to the performed linearization, the generalized elastic forces (18) are not in equilibrium with other loads. To enforce equilibrium a modified Newton–Raphson iteration is employed in the procedure here described; this requires computation of actual elastic forces at time  $t + \Delta t$ . To do this, local internal forces are first computed according to the elastic properties of the bar and to local co-ordinates as evaluated at time  $t + \Delta t$ , i.e.:

$${}^{t+\Delta t}N = k_{11} {}^{t+\Delta t}v_1; \quad {}^{t+\Delta t}V = k_{22} {}^{t+\Delta t}v_2 = k_{22} {}^{t+\Delta t}u_3 \quad (23)$$

where  ${}^{t+\Delta t}v_1$  can be evaluated from Equation (5) applied at time  $t + \Delta t$ .

Once local forces are computed, generalized forces can be obtained upon substitution in Equation (21).

**2.2.1. Computation of the element mass matrix and static nodal loads.** The mass matrix has been computed upon linearization of the bar displacement field about its undeformed configuration; this choice of the reference configuration is justified by considering that the anchor rods are designed so that in the static equilibrium configuration gravity and buoyancy loads give raise to a ‘neutral’ condition in which the bar is practically straight.

To express the element absolute velocity field the local co-ordinate system  $\bar{\mathbf{u}}$  can be first considered (Figure 5); under the above linearization criterion and consistently with the shape functions adopted for stiffness formulation, the bar velocity components along local co-ordinate axes are simply obtained, by time differentiation, in the form

$$\dot{\bar{v}}_x = \dot{\bar{u}}_2(1 - x/L) + \dot{\bar{u}}_5 x/L, \quad \dot{\bar{v}}_y = \dot{\bar{u}}_1(1 - x/L) + \dot{\bar{u}}_4 x/L + \dot{\bar{u}}_3 \sin(\pi x/L) \quad (24)$$

When the bar kinetic energy is written the local element mass matrix  $\mathbf{m}$  can be readily expressed as follows:

$$T = \frac{1}{2} \int_0^L \gamma (\dot{\bar{v}}_x^2 + \dot{\bar{v}}_y^2) dx = \frac{1}{2} \dot{\bar{\mathbf{u}}}^T \mathbf{m} \dot{\bar{\mathbf{u}}} \quad (25)$$

where the mass per unit length  $\gamma$  has been introduced.

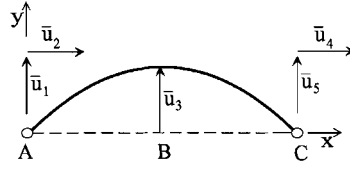


Figure 5. Local co-ordinate system for anchor element.

To get the element mass matrix  $\mathbf{M}$  in the global reference frame a standard transformation accounting for the rotation  $\theta$  of the element axis can be easily performed; such transformation does not affect the midspan relative deflection, since  $\dot{u}_3 = \dot{\bar{u}}_3$ . The matrix obtained is given in the Appendix.

Finally, consistent static nodal loads have been derived, under the same hypotheses as adopted for inertia loads, to take into account element weight and buoyancy.

### 2.3. Element loads due to hydrodynamic effects

Aim of the analysis is the simulation of the dynamic response of a floating tunnel under extreme transverse and vertical seismic loads; 'normal' sea waves, acting in transverse direction as well are superimposed on earthquake effects. In the light of this, wave loading was introduced according to a very simple model; has been first assumed that the wave field can be modelled according to the Airy linear theory [5]. The horizontal ( $Y$  direction) and vertical ( $Z$  direction) components of water velocity can be thus expressed by the following formulae:

$$\dot{w}_Y = \frac{\omega H}{2} \frac{\cosh(kZ)}{\sinh(kh)} \cos(kY - \omega t) \quad (26a)$$

$$\dot{w}_Z = \frac{\omega H}{2} \frac{\cosh(kZ)}{\sinh(kh)} \sin(kY - \omega t) \quad (26b)$$

where  $H$  is the wave height,  $h$  the water depth,  $\omega$  the wave circular frequency and  $k$  the wave number. The latter quantities are related to wave period  $T$ , wavelength  $\lambda$  and wave velocity  $c$  through the well-known expressions

$$k = 2\pi/\lambda, \quad \omega = 2\pi/T, \quad c = \omega/k = \lambda/T$$

where the following relation between  $\omega$  and  $k$  holds

$$\omega^2 = gk \tanh(kh)$$

To express the wave force acting upon an inclined submerged element lying in the ( $Y, Z$ ) plane the Morison approach as generalized by Chakrabarty was adopted; accordingly (see again Reference [5]), with reference to the local ( $x, y$ ) of Figure 5, the force per unit length acting in the direction normal to the element axis is given by the generalized Morison equation

$$f_y(x, t) = \frac{1}{2} \rho D C_D |\dot{w}'_y(x, t)| \dot{w}'_y(x, t) + \rho C_I \frac{\pi D}{4} \ddot{w}_y(x, t) - \rho(C_I - 1) \frac{\pi D^2}{4} \ddot{v}_y(x, t) \quad (27)$$



where the following symbols have been introduced:

- $\rho$  is the water density,  
 $D$  is the element diameter,  
 $C_D, C_I$  are the element drag and inertia coefficients,  
 $\dot{w}'_y = \dot{w}_y - \dot{v}_y$  is the relative velocity, defined as the difference between the normal component  $\dot{w}_y$  of the water velocity and the normal component  $\dot{v}_y$  of the structure velocity.

To simplify Equation (27) two assumptions are made. First the structure velocity is assumed to be small w.r.t. the water velocity so that the drag term can be written as

$$\frac{1}{2} \rho D C_D |\dot{w}'_y| \dot{w}'_y \simeq \frac{1}{2} \rho D C_D (|\dot{w}_y| \dot{w}_y - 2 |\dot{w}_y| \dot{v}_y) \quad (28)$$

Secondly the instantaneous absolute value  $|\dot{w}_y|$  of water particle velocity is approximated by an average value  $\hat{\omega}_y$ ; this is computed in order to minimize the error in a least square sense. To do this the integral

$$I = \int_0^{2\pi} (|\dot{w}_y| \dot{w}_y - \hat{\omega}_y \dot{w}_y)^2 d(\omega t)$$

is minimized, obtaining

$$\hat{\omega}_y = \frac{8}{3\pi} \frac{\omega H}{2} \frac{\sqrt{\sin^2 \theta + \sinh^2(kZ)}}{\sinh(kh)} \quad (29)$$

With the above criteria Equation (27) simplifies to the following form:

$$\begin{aligned} f_y(x, t) = & \frac{1}{2} \rho D C_D \hat{\omega}_y \dot{w}_y(x, t) + \rho C_I \frac{\pi D^2}{4} \ddot{w}_y(x, t) \\ & - \rho D C_D \hat{\omega}_y \dot{v}_y(x, t) - \rho (C_I - 1) \frac{\pi D^2}{4} \ddot{v}_y(x, t) \end{aligned} \quad (30)$$

in which the first term represents the linearized drag loading, the second the inertia loading, the third the added damping effect and the last the added mass effect. The added damping value was almost negligible, in the examples here studied, in comparison with structural dissipation; this was mainly due to the small value of average water velocity  $\hat{\omega}_y$  resulting from tunnel placement (40 m below water table).

The distributed load (30) has been treated by means of a lumped parameter approach; to do this transverse concentrated loads acting at the element ends (points A and C in Figure 5) and at midspan (point B) have been simply computed as follows:

$$F_y^{(A)} = f_y(0, t) \frac{L}{4}, \quad F_y^{(C)} = f_y(L, t) \frac{L}{4}, \quad F_y^{(B)} = f_y(L/2, t) L/2 \quad (31)$$

The generalized components of these forces referred to the element co-ordinates  $\mathbf{u}$ , i.e. the equivalent nodal load, added damping and mass coefficients, have been subsequently computed

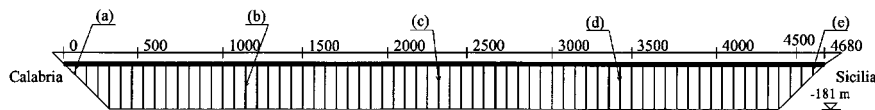


Figure 6. Side view of floating tunnel (Example B).

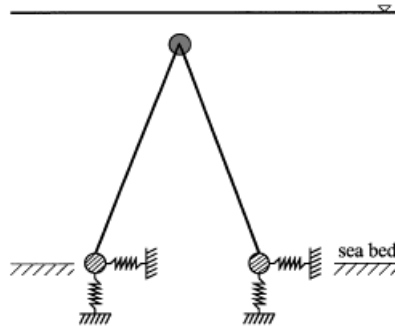


Figure 7. Simplified model of anchor system.

by means of standard structural analysis manipulation based upon the virtual work done by the force themselves.

The formulation of hydrodynamic loads due to steady current effects is under development.

#### 2.4. Model validation

The performance of the proposed finite element have been tested against the results obtained, for a plane problem resembling a segment of the tunnels at study, by using the general purpose finite-element code ABAQUS [6]; the properties of the test system are described in Figure 8. Different FE discretizations of the anchor bars were tested, based upon the hybrid cubic three-node element B23H; large displacement and deformation analysis was performed. The results obtained are shown in detail in Reference [7]; in Figure 9 an example of is given, showing the time histories of the horizontal displacement of the lumped mass as computed via the proposed model and via the ABAQUS procedure. As can be noted, the best match between the results is obtained by discretizing the anchor rods with four B23H beam elements. With such discretization the ratio between computing times is about 50 for a 20 s long dynamic analysis under seismic excitation.

### 3. COMPUTATION OF TUNNEL RESPONSE TO SEISMIC EXCITATION

#### 3.1. Equations of motion and solution strategies

To assess the structural response of a soil–structure system having plane dimensions of the order of some kilometers, multiple-support excitation effects are to be taken into account. To this end,

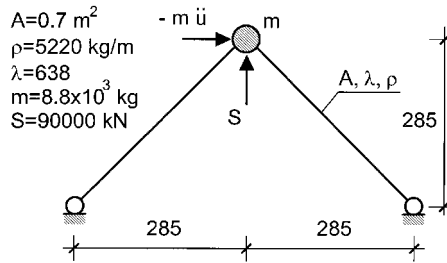


Figure 8. Example for finite element validation.

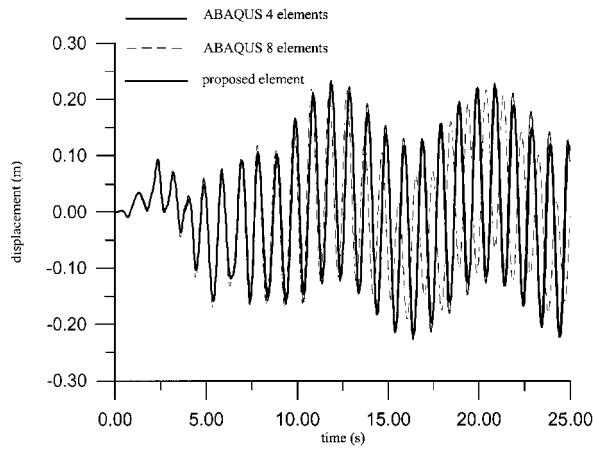


Figure 9. Finite element validation: comparison with ABAQUS results.

the following hypotheses have been adopted:

- (1) the mechanical behaviour of soil is linear,
- (2) soil–structure interaction effect can be modelled by means of a lumped-parameter approach in which soil behaviour is represented by springs and dashpots having frequency-independent properties.

Accordingly, the dynamic equilibrium equations for the soil–structure system can be written [8] in the partitioned form:

$$\begin{aligned}
 & \begin{bmatrix} \mathbf{M}_{ss}^{(s)} + \mathbf{M}_{ss}^{(h)} & \mathbf{M}_{sc}^{(s)} + \mathbf{M}_{sc}^{(h)} \\ \mathbf{M}_{cs}^{(s)} + \mathbf{M}_{cs}^{(h)} & \mathbf{M}_{cc}^{(s)} + \mathbf{M}_{cc}^{(h)} \end{bmatrix} \begin{Bmatrix} \ddot{\mathbf{q}}_s \\ \ddot{\mathbf{q}}_c \end{Bmatrix} + \begin{bmatrix} \mathbf{C}_{ss}^{(s)} + \mathbf{C}_{ss}^{(h)} & \mathbf{C}_{sc}^{(s)} + \mathbf{C}_{sc}^{(h)} \\ \mathbf{C}_{cs}^{(s)} + \mathbf{C}_{cs}^{(h)} & \mathbf{C}_{cc}^{(s)} + \mathbf{C}_{cc}^{(h)} + \mathbf{C}_{cc}^{(g)} \end{bmatrix} \begin{Bmatrix} \dot{\mathbf{q}}_s \\ \dot{\mathbf{q}}_c \end{Bmatrix} \\
 & + \begin{bmatrix} \mathbf{K}_{ss}^{(s)} & \mathbf{K}_{sc}^{(s)} \\ \mathbf{K}_{cs}^{(s)} & \mathbf{K}_{cc}^{(s)} + \mathbf{K}_{cc}^{(g)} \end{bmatrix} \begin{Bmatrix} \mathbf{q}_s \\ \mathbf{q}_c \end{Bmatrix} = \begin{Bmatrix} \mathbf{R}_s^{(s)} \\ \mathbf{R}_c^{(s)} \end{Bmatrix} + \begin{Bmatrix} \mathbf{0} \\ \mathbf{C}_{cc}^{(g)} \dot{\mathbf{q}}_c^{(f)} \end{Bmatrix} + \begin{Bmatrix} \mathbf{0} \\ \mathbf{K}_{cc}^{(g)} \mathbf{q}_c^{(f)} \end{Bmatrix} + \begin{Bmatrix} \mathbf{Q}_s \\ \mathbf{Q}_c \end{Bmatrix} \quad (32)
 \end{aligned}$$

where the following notations apply:

$\mathbf{q}$	is the vector of Lagrangian co-ordinates, represented here by generalized absolute displacements,
$s, c$	are the subscripts denoting respectively the displacements $\mathbf{q}_s$ of structural nodes, and displacements $\mathbf{q}_c$ of 'contact' nodes, located at the ground-structure interface,
(f)	is the superscript indicating free-field motion,
$\mathbf{M}, \mathbf{C}, \mathbf{K}$	are the inertia, damping and elastic stiffness matrices respectively,
$\mathbf{R}$	is the vector of generalized non-linear restoring forces,
(g), (s), (h)	are the superscripts denoting respectively ground, structural and hydrodynamic (added mass and damping) contributions,
$\mathbf{Q}$	is the vector of generalized components of external loads (wave loads, buoyancy, dead weight).

It is also assumed that foundation embedment effects are negligible, so that the  $\mathbf{q}_c^{(f)}$  motion can be taken as equal to the surface free-field motion.

The solution of the non-linear equations of motion (32) is performed, within the procedure here described, by means of the step-by-step technique described in Reference [9]; this is an implicit procedure based upon classical solution strategies such as the Newmark method for time integration and the Modified Newton–Raphson (MNR) iterative algorithm for equilibrium correction.

### 3.2. Computation of structural damping matrix

The computation of a viscous damping matrix for complex soil–structure systems and excitation patterns, as the ones here at study, can be a difficult task; indeed, simplifying assumptions, such as the Rayleigh damping hypothesis, can lead to unreliable results, due to the fact that structural response can be spread over a significant band of frequency components. For this reason a more refined procedure is here proposed to build the damping matrix; to this end, it is first assumed that the ground contribution can be resolved into a hysteretic-type component  $\mathbf{C}^{(g,H)}$  (intrinsic damping) and a viscous-type component  $\mathbf{C}^{(g,V)}$  (radiation damping). If structural damping is in turn assumed to be of hysteretic type the total soil–structure damping can be written as the sum of hysteretic and viscous effects, that is:

$$\mathbf{C}^{(s)} + \mathbf{C}^{(g)} = \mathbf{C}^{(s)} + \mathbf{C}^{(g,H)} + \mathbf{C}^{(g,V)} = \mathbf{C}^{(H)} + \mathbf{C}^{(V)} \quad (33)$$

where

$$\mathbf{C}^{(H)} = \mathbf{C}^{(s)} + \mathbf{C}^{(g,H)}, \quad \mathbf{C}^{(V)} = \mathbf{C}^{(g,V)} \quad (34)$$

No problem arises for the determination of the viscous ground matrix  $\mathbf{C}^{(g,V)}$ , which directly stems from foundation impedance; to build the matrix  $\mathbf{C}^{(H)}$  it is assumed that the soil–structure hysteretic-type damping is proportional. Accordingly, the following steps are performed.

- (1) A reduced linear model of the soil–structure system is set neglecting the transverse relative displacement of the anchor bars, which are modelled via a single truss element with geometric stiffness; added mass is taken into account. The development of a reduced model is necessary in order to eliminate local modes due to transverse oscillations of anchor bars: damping of these oscillations will be treated subsequently.

- (2) The first  $p$  normal modes  $\phi_j^{(r)}$  and frequencies  $\omega_j^{(r)}$  of the reduced model are extracted.
- (3) Starting from the eigenpairs  $\phi_j^{(r)}, \omega_j^{(r)}$ , as is well known, it is possible to compute a (reduced) orthonormal damping matrix  $\bar{\mathbf{C}}^{(\text{Hr})}$  leading to prescribed values of the modal damping factors for as many normal modes as required [10]. This matrix, however, is a full one, thus resulting in untolerable increase in computational effort during the solution phase. To reduce the matrix  $\bar{\mathbf{C}}^{(\text{Hr})}$  to a banded structure, though preserving a good approximation in terms of modal damping factors, an iterative procedure was devised. At iteration  $k$  the following operations are performed.
  - (a) The full damping matrix is computed according to the summation [10]

$$\bar{\mathbf{C}}_k^{(\text{Hr})} = \mathbf{M}^{(r)} \left[ \sum_{j=1}^p \phi_j^{(r)} \phi_j^{(r)\text{T}} \frac{2\bar{\zeta}_{j,k} \omega_j^{(r)}}{M_j^{(r)}} \right] \mathbf{M}^{(r)} \quad (35)$$

where the superscript (r) denotes properties and eigenpairs of the reduced model,  $M_j^{(r)} = \phi_j^{(r)\text{T}} \mathbf{M}^{(r)} \phi_j^{(r)}$  is the  $j$ th modal mass and where at first iteration ( $k = 0$ ) the modal damping factors  $\bar{\zeta}_{j,k}$  are set to the 'target' value  $\zeta$  for all modes considered. Note that, in this way, the same amount of hysteretic damping is assumed for the structure and the foundation medium; if different values are prescribed, equivalent weighted modal factors can be computed (see Reference [11]) and fed into Equation (35).

- (b) The banded matrix  $\mathbf{C}_k^{(\text{Hr})}$  is computed, by simply setting to zero elements outside the half-bandwidth  $m$  in the full matrix  $\bar{\mathbf{C}}_k^{(\text{Hr})}$ .
- (c) The actual modal damping factors are computed:

$$\zeta_{j,k} = \frac{1}{2\omega_j^{(r)}} \frac{\phi_j^{(r)\text{T}} \mathbf{C}_k^{(\text{Hr})} \phi_j^{(r)}}{M_j^{(r)}}, \quad j = 1, \dots, p. \quad (36)$$

- (d) The level of approximation of the factors (36), defined as the RMS error

$$\varepsilon_k = \sqrt{\frac{1}{p} \sum_{j=1}^p \left( \frac{\zeta_{j,k} - \zeta}{\zeta} \right)^2} \quad (37)$$

is checked against a prescribed tolerance  $\bar{\varepsilon}$ . In the case of satisfactory level ( $\varepsilon_k < \bar{\varepsilon}$ )  $\mathbf{C}_k^{(\text{Hr})}$  is taken as damping matrix  $\mathbf{C}^{(\text{Hr})}$  (hysteretic-type contributions) of the reduced soil-structure system and the iterative procedure is ended.

- (e) In the case  $\varepsilon_k > \bar{\varepsilon}$ , corrected damping factors are evaluated according to the following rule:

$$\bar{\zeta}_{j,k+1} = \zeta^2 / \zeta_{j,k}, \quad j = 1, \dots, p \quad (38)$$

and the analysis goes back to step (a).

It is worth noting that the procedure is clearly not rigorous and that convergence cannot be demonstrated neither formally nor empirically; experience teaches that when approximation is still unsatisfactory after a few cycles, the iteration must be restarted on the basis of a larger bandwidth value.

- (4) The matrix  $\mathbf{C}^{(\text{Hr})}$  is expanded to the size of the complete model, by inserting damping terms associated with transverse displacement of anchor bars; since these are treated as relative co-ordinates (see Figure 4), only diagonal terms are added, whose values  $C_{jj}^{(\text{Ht})}$  are simply

computed as

$$C_{jj}^{(H)} = 2\zeta \sqrt{K_{jj}^0 M_{jj}} \quad (39)$$

where  $K_{jj}^0$  is the initial value of the transverse stiffness of the anchor element for which  $u_3 = q_j$ .

### 3.3. Generation of artificial ground motion

The integration of Equations (32) requires the knowledge of seismic motion time histories, in free-field conditions, at all soil–structure interface nodes. To this end a numerical procedure for artificial ground motion generation has been adopted [12], which is based upon the spectral representation method of Shinozouka [13, 14] and is developed in accordance with the criteria reported by Monti *et al.* [15].

Simulation is based on a stochastic model; the free-field surface acceleration at a point  $a(t)$  is modelled as an uniformly modulated non-stationary process. This can be expressed as the product of an ‘underlying’ stationary process  $\bar{a}(t)$  and of a deterministic envelope  $\eta(t)$ . To describe the underlying stationary acceleration at a site, the Kanai-Tajimi power spectral density (PSD) as modified by Clough and Penzien [16], is adopted, expressed as

$$S_{\bar{a}}(\omega) = S_0 \frac{1 + 4\zeta_g^2 \left(\frac{\omega}{\omega_g}\right)^2}{\left[1 - \left(\frac{\omega}{\omega_g}\right)^2\right]^2 + 4\zeta_g^2 \left(\frac{\omega}{\omega_g}\right)^2} \frac{\left(\frac{\omega}{\omega_f}\right)^4}{\left[1 - \left(\frac{\omega}{\omega_f}\right)^2\right]^2 + 4\zeta_f^2 \left(\frac{\omega}{\omega_f}\right)^2} \quad (40)$$

where  $S_0$  is a scale factor which can be related to peak ground acceleration,  $\omega_g$  and  $\zeta_g$  are the characteristic ground natural frequency and damping, while  $\omega_f$  and  $\zeta_f$  are the parameters of a highpass filter. The same model is assumed for all contact points, which means that global attenuation and site effects are disregarded.

Under such hypothesis, to describe the spatial variation of the ground motion the cross-spectral density between stationary acceleration at two sites located at a separation distance  $\xi$ , has been expressed as the product

$$S_{\bar{a}_{jk}}(\omega, \xi) = \gamma_{jk}(\omega, \xi) S_{\bar{a}}(\omega) \quad (41)$$

of the PSD (40) and of the coherency function  $\gamma_{jk}(\omega, \xi)$ ; for the latter a model was adopted which is able to represent both the ‘geometric incoherence’ effect, due to reflections and refractions of waves along the propagation path, and the ‘wave passage’ effect, due to the finite value of propagation velocity. The chosen model is due to Luco and Wong [17] and is defined by the following expression:

$$\gamma_{jk}(\omega, \xi) = \exp \left[ - \left( \frac{\omega \alpha \xi}{v_s} \right)^2 \right] \exp \left( i \omega \frac{\xi^{(L)}}{v_{app}} \right) \quad (42)$$

where  $v_s$  is the shear wave velocity,  $v_{app}$  is the surface apparent velocity of ‘dominant’ waves,  $\xi^{(L)}$  is the projection of the horizontal distance between the sites along the propagation direction and  $\alpha$  is a parameter controlling coherence decay.

Since constant apparent propagation velocity is assumed, the wave passage effect (complex factor in expression (42)) simply results in a delay of the wave arrival time at the different sites; this can be easily handled by the structural analysis procedure, so that the real factor only, related to geometric incoherence, has been retained in Equation (42) for the artificial generation.

Once a set of stationary acceleration segments has been generated according to expressions (41) and (42), to obtain the complete non-stationary ground motion field the following steps are performed.

- (1) Scaling of each acceleration time history by the following deterministic envelope:

$$\begin{aligned}\eta(t) &= \left(\frac{t}{t_1}\right)^2 \quad \text{for } 0 \leq t \leq t_1 \\ \eta(t) &= 1, \quad \text{for } t_1 < t \leq t_2 \\ \eta(t) &= \exp\left\{\frac{t - t_2}{t_{\max} - t_2} \ln \beta\right\}, \quad \text{for } t_2 < t \leq t_{\max}\end{aligned}\tag{43}$$

- (2) Double integration to get time histories of ground velocity and displacement, performed according to the frequency domain procedure described in Reference [18].

#### 4. EXAMPLES OF APPLICATION

##### 4.1. Structural modelling

The performance of the proposed procedure in handling a real case was tested by studying the seismic behaviour of two tunnel models; both of them are largely based on published data and design criteria [2] about the crossing of the Messina Strait between Punta S. Ranieri and Catona (4680 m). The difference between the two models is that in the first (shown in Figure 1 and called A in the following) the actual seabed profile is introduced with slight simplifications, while in the second (model B — Figure 6) constant water depth (equal to 181 m) is assumed for the largest part of the crossing.

Both models have a number of degrees of freedom  $n = 658$  and are based upon the following hypotheses and criteria:

- (1) The tunnel is modelled by means of 3D beam elements, neglecting axial deformation and torsional behaviour. The structural section is a composite steel-concrete thick pipe (external diameter 15.95 m, internal 13.95 m) having an equivalent area, referred to concrete elastic properties, of 58.24 m<sup>2</sup> and an equivalent moment of inertia of 1637 m<sup>4</sup>. Lumped masses are positioned at anchoring sections, having a 72 m constant spacing; weight per unit length of 1800 kN/m is considered. The assumed difference between buoyancy and weight is equal to 455 kN/m.
- (2) The actual anchoring system is modelled through a couple of equivalent elements having the same total area and slenderness of real bars; the elements, which are of the type described in Section 2, are located as shown in Figure 7. For model A the area of the elements ranges from 0.85 m<sup>2</sup> (end sections) to 0.7 m<sup>2</sup> (midspan sections); given the seabed

profile, slenderness values range from 66 to 638. For model B a constant area of  $0.77 \text{ m}^2$  is introduced; slenderness value is constant in the central part of the crossing and equal to 299.

- (3) Soil–structure interaction effects are accounted for by inserting two elastic springs (in the vertical and transverse direction) at the bottom of each anchor element; linear dashpots representing radiation effect are provided as well acting parallel to springs. Stiffness and damping constants computation (see Reference [19]) are based upon the hypothesis of a six-pile foundation block; the following values of block mass  $M_f$ , pile diameter  $\phi_p$ , pile length  $L_p$ , soil elastic shear modulus  $G_s$  and Poisson modulus  $\mu_s$  have been assumed

$$M_f = 2810 \text{ t}, \quad \phi_p = 2.5 \text{ m}, \quad L_p = 51 \text{ m}, \quad G_s = 118000 \text{ kN/m}^2, \quad \mu_s = 0.25$$

- (4) Damping factor equivalent to hysteretic effects  $\zeta$  (see Section 3.2) is assumed equal to 0.02 for both the structure and the ground. The procedure described in Section 3.2 was applied on the basis of the first 130 normal modes. A damping matrix bandwidth  $m = 35$ , equal to the one of the stiffness matrix, was introduced and four iterations were performed; final RMS error (37) was equal to  $5.2 \times 10^{-4}$  for model A and to  $8.5 \times 10^{-5}$  for model B. The largest error was 5.7 per cent for model A (actual damping factor of mode 113 equal to 0.01886) and 0.7 per cent for model B (actual damping factor of first mode equal to 0.01985).

#### 4.2. Environmental actions modelling

Wave loading on anchor elements is simulated according to the criteria described at Section 2.3. The same criteria were used for the tunnel; it is recognized that, given the tunnel section dimensions, justification of the Morison approach becomes questionable in this case. Nevertheless the Morison criterion has been here accepted here taking also into consideration the small influence of hydrodynamic damping; more refined techniques, however, are under study for more general applications. The following values of wave height  $H$ , wavelength  $\lambda$ , wave period  $T$ , inertia coefficient  $C_I$  and drag coefficient  $C_D$  are assumed:

$$H = 5 \text{ m}, \quad \lambda = 156, \quad T = 5 \text{ s}, \quad C_I = 2, \quad C_D = 1.2$$

As to seismic motion modelling, the following parameters were supplied for the definition of the stationary acceleration PSD (40) of the coherency function (42) and of the envelope function (43):

$$\omega_g = 10 \text{ rad/s}, \quad \zeta_g = 0.4, \quad \omega_f = 1 \text{ rad/s}, \quad \zeta_f = 0.6, \quad \alpha = 1$$

$$v_s = 3.5 \text{ km/s}, \quad v_{app} = 4.95 \text{ km/s}, \quad t_1 = 2 \text{ s}, \quad t_2 = 10 \text{ s}, \quad t_{max} = 40 \text{ s}, \quad \beta = 0.25$$

The assumed  $S_0$  value is consistent with a peak ground acceleration of  $0.64g$ ; apparent wave propagation goes from Calabria to Sicilia (Figures 1 and 6).

Note that the same stochastic properties are assumed for horizontal (perpendicular to the bridge axis) and vertical seismic motion. Independent generation of two sets of time histories, one set for the transverse component and the other one for the vertical one, was performed.

#### 4.3. Results of the analysis

Some of the results of the performed analyses are shown, in Figures 10–16, mainly for illustrating the procedure capabilities; nevertheless, some tentative interpretations of the results are given, even though the dynamic behaviour of the studied structures is very complex and most of its



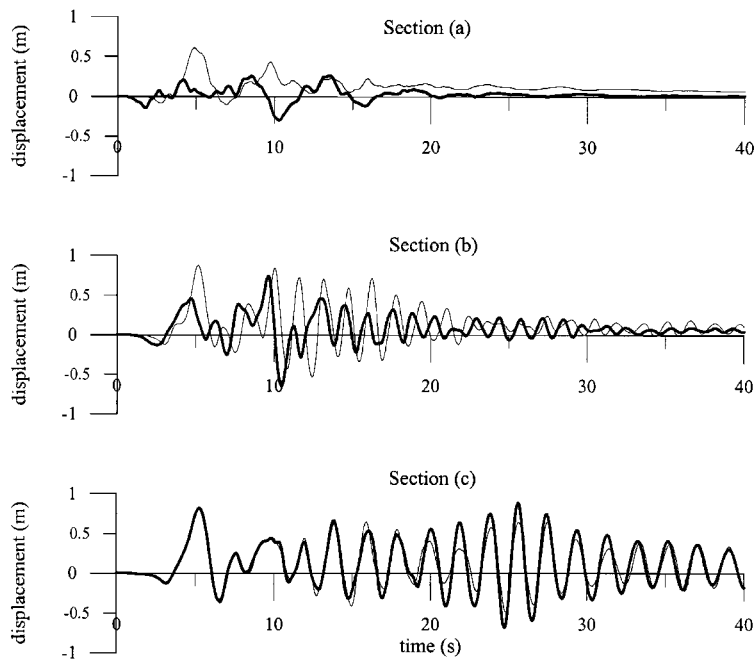


Figure 10. Time histories of tunnel horizontal displacement for Example A.

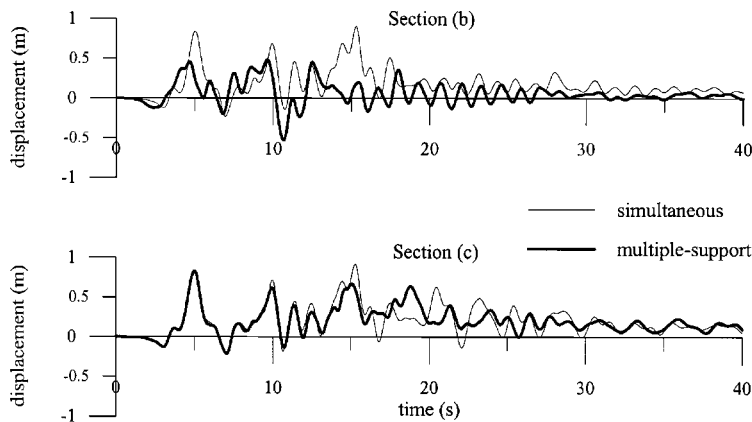


Figure 11. Time histories of tunnel horizontal displacement for Example B.

aspects deserve careful investigation before any conclusion of practical 'design-oriented' value can be drawn.

In Figure 10 time-histories of the tunnel horizontal displacement at sections 'a' through 'c' (see Figure 1) are given for model A; the cases of simultaneous and multiple-support seismic excitation

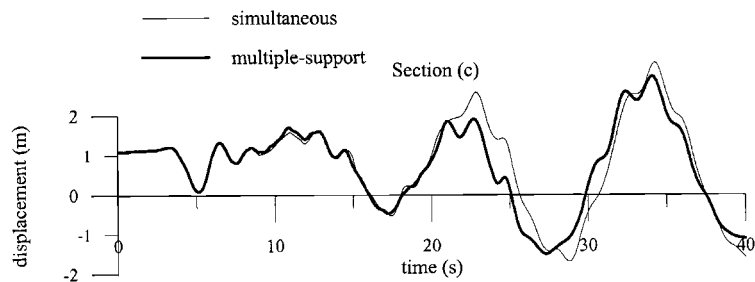


Figure 12. Time histories of relative transverse displacement of anchor rods on South side. Example A.

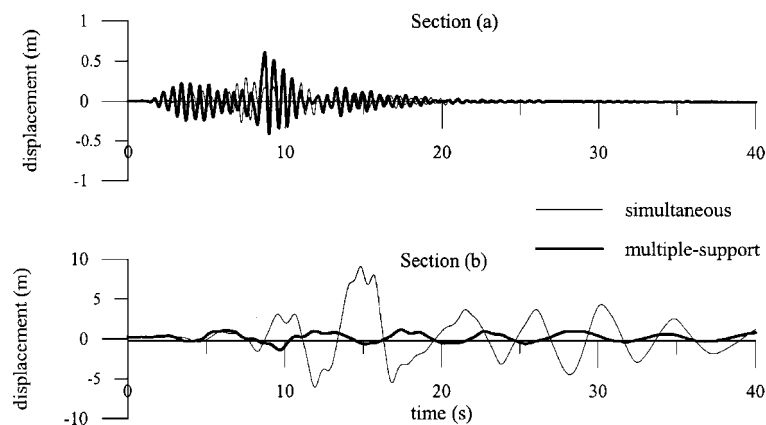


Figure 13. Time histories of relative transverse displacement of anchor rods on South side. Example B.

are both shown for comparison. In the simultaneous case, the time history generated for section 'c' is inputted at all support points. The displacement history appears to be dominated by frequency components around 0.5–0.7 Hz for  $t > 20$  s; these values are consistent with the lowest natural frequencies found for the determination of the structural damping matrix (see Section 3.2). Lower frequency contributions appear in the interval  $5 < t < 15$  s, where the strongest seismic motion occurs. The effect of multiple support excitation is not too significant; at section 'c', where seismic input is the same in the two cases, the tunnel response is practically identical within the strong motion phase. At section 'b' the overall response intensity is more severe in the simultaneous excitation case; the difference in terms of peak values is about 20 per cent.

In Figure 11 time histories are given, at sections 'b' and 'c', for example tunnel B (at section 'a' the response is practically identical to the one of Figure 10). It can be noted that at section 'b', where the anchor rod length is about the same in the two models, responses are rather similar, especially for the multiple-support input case. At midspan section 'c', on the contrary, responses are very different for the two examples; these considerations support the belief that 'local'

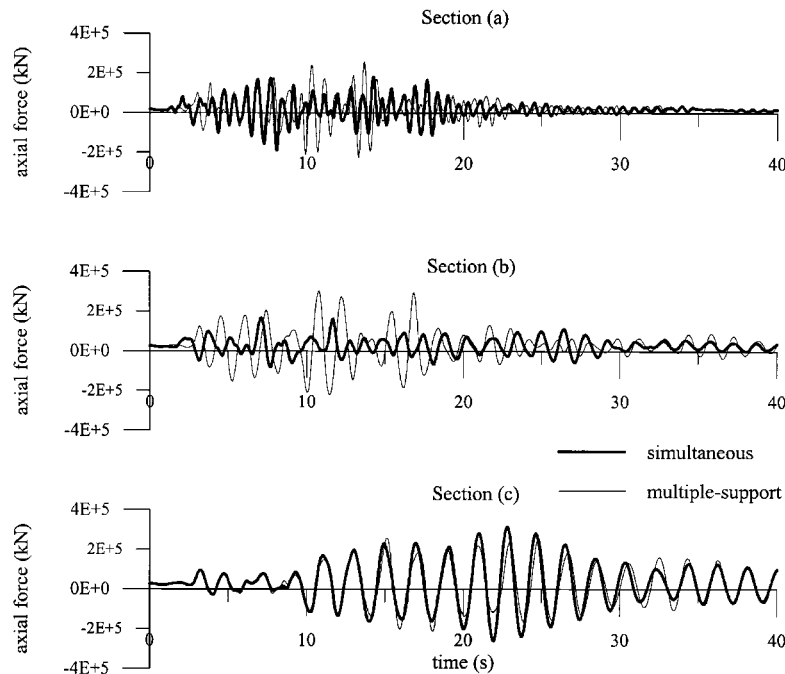


Figure 14. Time histories of axial force in anchor rods on South side. Example B.

behaviour, mainly influenced by the anchor rod slenderness, is the most important factor governing structural response. It can be also observed how the effect of multiple-support excitation is obviously much more marked for the regular tunnel (Example B).

Finally, some of the time-histories of Figures 10 and 11 show significant response drift; it must be reminded that total displacements are computed here, which are affected by ground displacement. Since the average value of velocity was not set to zero in the integration procedure performed within the simulation process (Section 3.3), while null initial ground motion was imposed, final ground displacements are possible; these are responsible for the permanent values of total structural drift.

Very similar considerations can be drawn looking at the vertical tunnel displacements, not shown here for brevity.

Figures 12 and 13 illustrate the time histories of relative transverse displacement of some of the anchor rods; note that different scaling of displacement axis was set due to very different motion intensities. More precisely, much larger amplitudes are detected for model B, especially in the simultaneous excitation case, where transverse displacement of about 9 m occur in most anchor rods; for multiple-support excitation similar values occur but in a limited number of sections.

Looking at Figure 12, where the behaviour of a very slender elements is given, the superposition of low and high frequency oscillations can be easily noted; the former are due to local transverse modes, while the latter, showing the same frequencies as observed for tunnel displacements, appear to be 'driven' by overall structural response. It is worth noting that high

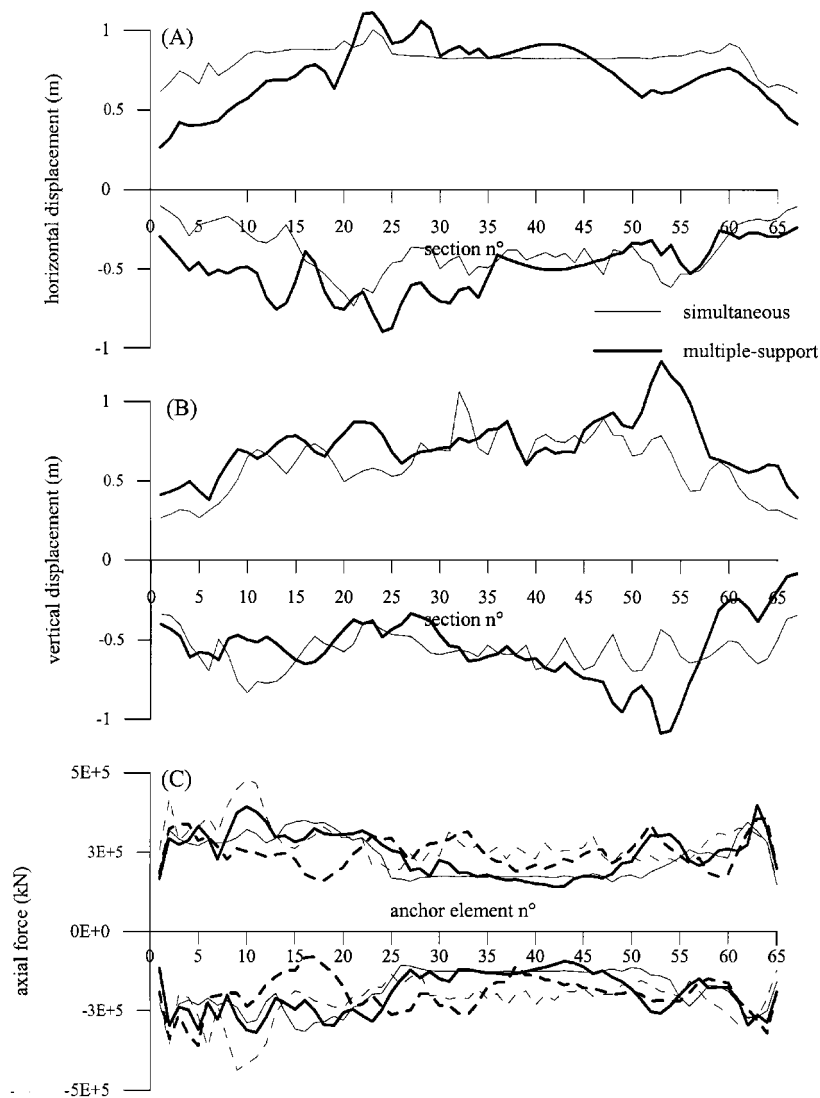


Figure 15. Envelopes of tunnel horizontal displacement (A), vertical displacement (B) and anchor rods axial force (C), continuous lines for North side anchor rods, dotted lines for South side anchor rods. Example A.

frequency components of local transverse response lead to high values of acceleration and velocity which in turn, given also the added inertia and damping properties coming from hydrodynamic effects, lead to the occurrence of significant transverse inertia and damping forces. These forces are responsible for the significant values of compressive loads which appear in Figure 14, where axial force time histories are not far from symmetric even for very slender elements. The occurrence of high compressive force in slender anchor rods is obviously one of the

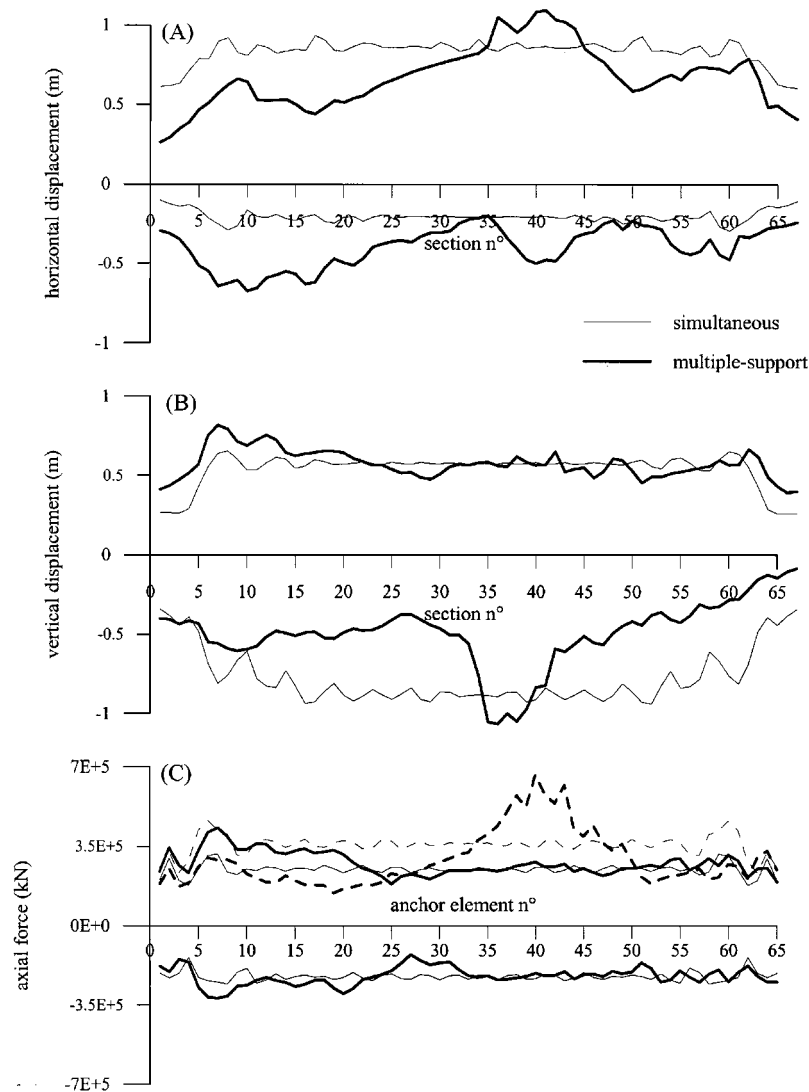


Figure 16. Envelopes of tunnel horizontal displacement (A), vertical displacement (B) and anchor rods axial force (C), continuous lines for North side anchor rods, dotted lines for South side anchor rods. Example B.

aspects which will be subject to further investigation; the possible activation of higher modes of transverse oscillation, for example, seems to deserve further study.

Figures 15 and 16 show, for both structures, the envelopes of maximum and minimum tunnel displacements and of anchor rods axial forces. Vertical and horizontal displacements are of the same order of magnitude, rarely exceeding 1 m. The effect of multiple support excitation on displacement extremes is not very well-defined and certainly needs further investigation.

Looking at structure A (Figure 15), a quite marked 'end-effect' is noted in terms of axial forces: maximum values exceed, in some cases, the yield limit, pointing out the need to extend the model to elastic-plastic material behaviour.

Computing time for each case was about ten minutes on a small-size RISC workstation.

## 5. CONCLUSIONS

A numerical procedure was set for the dynamic analysis of a seabed anchored floating tunnels under extreme seismic excitation. An 'ad hoc' finite element was developed for modelling the behaviour of anchor rods; the element, which accounts for geometrical non-linearities and wave loading, was inserted into a step-by-step integration procedure. This allows for the analysis of the dynamic response of non-linear structural systems, interacting with a linearly modelled foundation medium, under multiple-support seismic input. Particular attention was also devoted to the criteria for formulating the structural damping matrix.

As a preliminary test the procedure was applied to the analysis of the seismic behaviour of two 4680 m long example tunnels; the results obtained, though largely insufficient for engineering judgement of the structural behaviour, point out some of the facets of the dynamic response of the studied systems. For example, the results show how very slender anchor rods can resist, mainly due to inertial effects, significant compressive loads, this being an important aspect from the design view point.

Several further developments of the proposed methodology are possible; the extension of the element formulation to account for elastic-plastic material (actually in progress) and to 3D behaviour is anticipated, along with the consideration of steady current loads. Given the efficiency demonstrated by the numerical procedure it is possible to predict that even complete 3D materially non-linear analyses of complex floating tunnels will be feasible and that computing times will allow for the use of the procedure within a practical design process.

## APPENDIX A

$$K_L = \frac{EJ}{L^3} \begin{bmatrix} \lambda^2 R^2 & \lambda^2 RS & \frac{\pi^2}{2L} u_3 \lambda^2 R & -\lambda^2 R^2 & -\lambda^2 RS \\ & \lambda^2 S^2 & \frac{\pi^2}{2L} u_3 \lambda^2 S & -\lambda^2 RS & -\lambda^2 S^2 \\ \text{sim.} & & \frac{\pi^4}{2} \left( 1 + \frac{u_3^2}{2L} \lambda^2 \right) & -\frac{\pi^2}{2L} u_3 \lambda^2 R & -\frac{\pi^2}{2L} u_3 \lambda^2 S \\ & & & \lambda^2 R^2 & \lambda^2 RS \\ & & & & \lambda^2 S^2 \end{bmatrix}$$

where  $R = -\sin \theta + (u_1 - u_4)/L$ ;  $S = -\cos \theta + (u_2 - u_5)/L$

$$\mathbf{M} = \frac{\gamma L}{6} \begin{bmatrix} 2 & 0 & \frac{6}{\pi} c & 1 & 0 \\ & 2 & -\frac{6}{\pi} s & 0 & 1 \\ \text{sim.} & & 3 & \frac{6}{\pi} c & -\frac{6}{\pi} s \\ & & & 2 & 0 \\ & & & & 2 \end{bmatrix} \quad s = \sin \theta; c = \cos \theta$$

#### ACKNOWLEDGEMENTS

The authors wish to thank Professor Giulio Ballio of the Department of Structural Engineering of Politecnico di Milano for his scientific support to this research work.

#### REFERENCES

1. Brancaleoni F, Castellani A, D'Asdia P. The response of submerged tunnels to their environment. *Engineering Structures* 1989; **11**:47–56.
2. Bruschi R, Giardinieri V, Marazza R, Merletti T. *Submerged Buoyant anchored Tunnels: Technical Solution for the Fixed Link Across the Strait of Messina Strait Crossings*. Balkema: Rotterdam, 1990.
3. Bruschi R, Marazza R, Leira BJ. Submerged buoyant anchored tunnels: response analysis for earthquake: *Structural Dynamics-Eurodyn*, vol. 9, Balkema: Rotterdam, 1993.
4. Bathe KJ. *Numerical Methods in Engineering Analysis*. Prentice-Hall: Englewood Cliffs, NJ, 1982.
5. Dawson TH. *Offshore Structural Engineering*. Prentice-Hall: Englewood Cliff, NJ, 1983.
6. *ABAQUS User's and Theory Manuals. Release 5.6*. Hibbit, Karlsson & Soresen Inc., 1996.
7. Fogazzi P. Modellazione del comportamento sismico di elementi strutturali in acciaio soggetti a fenomeni d'instabilit . *Ph.D. Thesis*, Dipartimento di Ingegneria Strutturale, Politecnico di Milano, Milano, Italy, 1997 (in Italian).
8. Wolfe JP. *Dynamic Soil-Structure Interaction*. Prentice-Hall: Englewood Cliffs, NJ, 1985.
9. Perotti F, De Amici A, Venturini P. Numerical analysis and design implications of the seismic behaviour of one-storey steel bracing systems. *Engineering Structures* 1996; **18**(2):162–178.
10. Wilson EL, Penzien J. Evaluation of orthogonal damping matrices. *International Journal for Numerical Methods in Engineering* 1972; **4**(1):5–10.
11. Feriani A, Perotti F. The formation of viscous damping matrices for the dynamic analysis of M.D.O.F. systems. *Earthquake Engineering and Structural Dynamics* 1996; **25**:689–709.
12. Martinelli L. Implementazione di un metodo numerico per la generazione di storie di accelerazione per strutture a grandi dimensioni in pianta. *Ph.D. Thesis* (in partial fulfillment). Dipartimento di Ingegneria Strutturale, Politecnico di Milano, Milano, Italy, 1996 (in Italian).
13. Shinozuka M. Monte Carlo solution of structural dynamics. *Computer and Structures* 1972; **2**:855–874.
14. Shinozuka M. Digital simulation of random processes and its applications. *Journal of Sound and Vibration* 1972; **111**:11–128.
15. Monti G, Nuti C, Pinto PE. Nonlinear response of bridges under multisupport excitation. *ASCE Journal of Structural Engineering* 1996; **22**(10):1147–1159.
16. Ruiz P, Penzien J. Probabilistic study of the behaviour of structures during earthquakes. Earthquake Engineering Research Center, University of California, Berkeley, CA, 1969.
17. Luco JE, Wong HL. Response of a rigid foundation to a spatially random ground motion. *Earthquake Engineering and Structural Dynamics* 1986; **14**:891–908.
18. Perotti F. Frequency domain analysis of strong-motion accelerograms. Dipartimento di Ingegneria Strutturale del Politecnico di Milano, *T.R. N. 3/87*, 1987.
19. Moore PJ. *Analysis and Design of Foundations for Vibrations*. A.A. Balkema Publishers: Rotterdam, 1985.